INSTITUTE OF PHYSICS PUBLISHING PHYSICS IN MEDICINE AND BIOLOGY

Phys. Med. Biol. **50** (2005) 5229–5249 doi:10.1088/0031-9155/50/22/002

Monte Carlo simulations of a nozzle for the treatment of ocular tumours with high-energy proton beams

Wayne Newhauser[1,2], Nicholas Koch[1,2], Stephen Hummel[1], Matthias Ziegler[1,3] and Uwe Titt[1,4]

[1] The University of Texas M D Anderson Cancer Center, 1515 Holcombe Blvd, Houston, TX, USA
[2] The University of Texas Graduate School of Biomedical Sciences at Houston, 6767 Bertner Street, Houston, TX, USA
[3] University of California, 7523 Boelter Hall, Los Angeles, CA, USA
[4] Massachusetts General Hospital, 55 Fruit Street, Boston, MA, USA

E-mail: wnewhaus@mdanderson.org

Received 23 February 2005, in final form 24 August 2005
Published 24 October 2005
Online at stacks.iop.org/PMB/50/5229

Abstract

By the end of 2002, 33 398 patients worldwide had been treated with proton radiotherapy, 10 829 for eye diseases. The dose prediction algorithms used today for ocular proton therapy treatment planning rely on parameterizations of measured proton dose distributions, i.e., broad-beam and pencil-beam techniques, whose predictive capabilities are inherently limited by severe approximations and simplifications in modelling the radiation transport physics. In contrast, the Monte Carlo radiation transport technique can, in principle, provide accurate predictions of the proton treatment beams by taking into account all the physical processes involved, including coulombic energy loss, energy straggling, multiple Coulomb scattering, elastic and nonelastic nuclear interactions, and the transport of secondary particles. It has not been shown, however, whether it is possible to commission a proton treatment planning system by using data exclusively from Monte Carlo simulations of the treatment apparatus and a phantom. In this work, we made benchmark comparisons between Monte Carlo predictions and measurements of an ocular proton treatment beamline. The maximum differences between absorbed dose profiles from simulations and measurements were 6% and 0.6 mm, while typical differences were less than 2% and 0.2 mm. The computation time for the entire virtual commissioning process is less than one day. The study revealed that, after a significant development effort, a Monte Carlo model of a proton therapy apparatus is sufficiently accurate and fast for commissioning a treatment planning system.

1. Introduction

Melanoma of the uveal tract is the most common primary intraocular malignancy and the only potentially fatal intraocular tumour in adults. There are two major types of radiotherapy for the treatment of uveal melanoma: radioactive plaques that are sutured to the sclera over the area of the tumour (cf Stallard (1968)) and external-beam radiotherapy using charged particles, such as protons or helium ions. Proton radiotherapy, initially proposed by Wilson (1946), was recognized by Constable and Koehler (1974) to be well suited for treating intraocular neoplasms. Large proton doses can be delivered to the tumour volume, and the uninvolved intraocular and orbital structures can be largely spared, reducing the frequency or severity of treatment-related side effects, such as vision loss and the need for post-treatment enucleation when compared with plaque therapy (cf Munzenrider *et al* (1989), Gragoudas and Lane (2005)). Currently, 13 centres worldwide treat ocular or orbital diseases with proton beams.

In recent years the Monte Carlo technique for simulating radiation transport has become increasingly well suited to modelling proton therapy beams. For many simulation problems that were even recently considered intractable, simulation times have shrunk to manageable levels owing to improvements in the efficiency of Monte Carlo algorithms and to increasing computational power. In addition, most modern Monte Carlo radiation transport codes now realistically model all of the important physical processes, including coulombic energy loss, energy straggling, multiple Coulomb scattering, elastic and inelastic scattering, and nonelastic nuclear reactions (e.g. the production of secondary particles). These advances have spurred a rapid expansion of literature on Monte Carlo applications in proton therapy literature.

By taking into account beam-modifying devices upstream of the patient collimator, detailed beam characteristics and dose distributions can be estimated. Urie *et al* (1986) used simple, two-dimensional Monte Carlo simulations to investigate factors that influence the penumbra of the Harvard Cyclotron Laboratory (Cambridge, MA, USA) proton beam. Their simulations examined the influence of the configuration of the beam-shaping devices (i.e., collimating aperture and range compensators) on the penumbral characteristics. Romero *et al* (1995) compared Monte Carlo simulations and measurements of proton transmission images that could be used to help align a proton therapy patient with respect to the treatment field. Medin and Andreo (1997) simulated proton transport in water in order to estimate water-to-air mass stopping power ratios needed to interpret ionization chamber measurements of absorbed dose in proton therapy beams. Agosteo *et al* (1998) simulated the secondary radiation doses to proton therapy patients. Paganetti (1998a, 1998b) used Monte Carlo simulations to provide a detailed account of the proton fluence and the relative biological effectiveness of ocular proton therapy beams. Siebers (2000) benchmarked two Monte Carlo codes, the Los Alamos High Energy Transport Code (LAHET) (Prael and Lichtenstein 1989) and the Monte Carlo N-Particle Transport Code (MCNPX) (Hughes *et al* 1997), against beamline measurements and simulated patient-specific dose distributions for a proton radiotherapy prostate cancer treatment. In that study, Siebers modelled the Loma Linda University Medical Center's gantry beamline configured for a laterally-opposed field arrangement. Sakae *et al* (2000) designed a passive, multi-layer energy filter for conforming the proton field's high dose region, in three dimensions, to the target volume. Verhaegen and Palmans (2001) simulated correction factors for the perturbation effect that occurs in cavity ionization chamber measurements of proton therapy beams. Newhauser *et al* (2002b) and Titt and Newhauser (2005) compared simulations from MCNPX and measurements of the neutron fields throughout an operating proton therapy facility, demonstrating the feasibility of applying a general purpose Monte Carlo code to solve large-scale simulation problems in proton therapy. Schneider *et al* (2002) predicted and measured the secondary neutron dose to patients receiving scanned beam proton therapy.

Palmans *et al* (2002a, 2002b) have calculated fluence correction factors for plastic phantoms and correction factors for parallel plate ionization chambers for proton beam measurements. Jiang and Paganetti (2004) extended the GEANT Monte Carlo code for CT-voxel based proton therapy calculations in a manner similar to the earlier work of Siebers (2000). Fippel and Soukup (2004) have developed a Monte Carlo code especially for proton radiation therapy that is more than an order of magnitude faster than the general purpose GEANT and FLUKA codes. Paganetti *et al* (2004a, 2004b) reported simulated absorbed dose profiles that agreed well with measurements and extended the GEANT code to model a time-dependent geometry and source. Tourovsky *et al* (2005) have reported on a Monte Carlo algorithm with simplified physics models that provides sufficient accuracy for planning scanned-proton-beam treatments. Fontenot *et al* (2005) benchmarked Monte Carlo predictions of the radiosurgery nozzle from the Harvard Cyclotron Laboratory against measurements. Polf and Newhauser (2005) and Polf *et al* (2005a, 2005b) benchmarked Monte Carlo simulations of absorbed dose and neutron dose equivalent against measurements from the Harvard Cyclotron Laboratory's large-field proton therapy nozzle. Bues *et al* (2005) reported on simulated dose distributions obtained in a proton therapy field that was laterally shaped with a multi-leaf collimator. Schulte *et al* (2005) studied the limits of proton beam computed tomography using Monte Carlo simulations. Wroe *et al* (2005) simulated proton depth dose curves to study the influence of non-elastic nuclear reactions.

The literature pertaining to the application of the Monte Carlo technique to ocular proton therapy is extremely limited. Hérault *et al* (2005) simulated ocular proton dose distributions and output factor values with MCNPX for the Centre Antoine Lacassagne proton therapy center and found a good agreement with measurements. Koch and Newhauser (2005) reported on simulations with MCNPX of a double scattering ocular nozzle and used the simulation results to commission a proton therapy treatment planning system. In addition, they carried out treatment plans for an ocular melanoma case using both the Monte Carlo method and an analytical model in the treatment planning system. Mourtada *et al* (2005) carried out a comparative treatment planning study for a typical ocular melanoma case using proton beam therapy, radioactive ^{106}Ru/^{106}Ru and ^{125}I plaques, where the proton treatment planning was carried out with methods of Koch and Newhauser.

It has long been recognized, although never demonstrated, that the Monte Carlo method is capable of generating a sufficiently complete and accurate set of data for commissioning a treatment planning system. Taken together, the recent reports of Hérault *et al* and Koch and Newhauser strongly suggest that it should be possible to commission an ocular treatment planning system. Hérault *et al*, however, did report on treatment planning aspects and Koch and Newhauser did not report on validating the accuracy of the simulation results against measurements.

The current study aims to determine whether it is possible to commission a proton treatment planning system (TPS) using data exclusively from Monte Carlo simulations of the treatment apparatus and a phantom. In addition, we assessed the accuracy of depth and cross-field dose predictions from Monte Carlo simulations by comparing them with measurements from an ocular proton treatment beam. We also determined the computation times required for the Monte Carlo simulations.

2. Methods and materials

2.1. Nozzle geometry, materials, proton source model and dose estimates

The proton therapy nozzle's main purpose is to modify the small-diameter, 159 MeV proton beam in order to produce a dose distribution that is suitable for treating ocular tumours. This

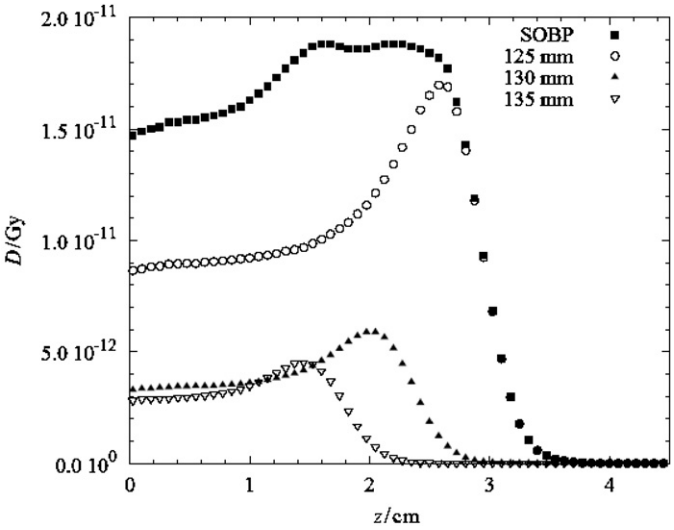

Figure 1. Central axis absorbed dose D per source proton as a function of water depth z. The spread-out Bragg peak (SOBP) (upper curve) is produced using fluence and range modulation. The individual pristine peaks (lower curves) are shown as $D(z)$ times their respective fluence weighting factors (the corresponding combined degrader/modulator thickness for each pristine curve is indicated in the legend). All of the profiles were simulated with an initial mean proton energy of 159 MeV and a Gaussian relative energy width of $\Delta E/E = 2.2\%$.

is achieved by laterally spreading a narrow raw proton beam to cover a tumour, by adjusting the maximum proton penetration depth (typical ocular melanoma treatments require 25 mm of beam penetration), and by modulating the proton beam range and fluence to produce a uniform dose distribution at the required depths. Figure 1 plots an example of a range-modulated or spread-out Bragg peak (SOBP) along with the individual constituent pristine Bragg peaks.

The energy distribution of the raw proton beam, i.e., as it enters the ocular nozzle, is needed in order to model the nozzle with the Monte Carlo method. It was not measured directly, but deduced by finding the best agreement in the shape of the measured and ten simulated Bragg curves in water. For the simulated Bragg curves, the mean initial proton energy was held constant at 159 MeV, the initial energy distribution was assumed to be Gaussian, and the relative energy width ($\Delta E/E$, or the full-width at half-maximum (FWHM) divided by the mean initial energy) was varied from 0% (mono-energetic) to 3.33%. Laterally, the spatial distribution of the intensity of the raw beam was approximated using a radially symmetric Gaussian profile of 5 mm FWHM based on measurements of the Harvard raw proton beam size.

In the Monte Carlo model of the ocular beamline that we used, the raw beam first traverses 100 mm of air before entering the nozzle. Figure 2 shows the nozzle (after Newhauser *et al* (2001, 2002a)) and the corresponding geometric model in this work. Nozzle components, materials and dimensions are listed in table 1. The beam is incident upon a brass collimator, a rotating range modulator wheel made of Lucite ($C_5H_8O_2$, $\rho \approx 1.19$ g cm^{-3}, GE Plastics Inc, Pittsfield, MA), a fixed degrader made of Lexan ($C_{16}H_{14}O_3$, $\rho \approx 1.20$ g cm^{-3}, GE Plastics Inc, Pittsfield, MA), a Lexan variable degrader, a pair of monitor ionization chambers, a brass snout, and a final beam-shaping aperture of brass. The brass used in these simulations is 61.5% copper, 35.2% zinc and 3.3% lead, and has a density of 8.49 g cm^{-3}.

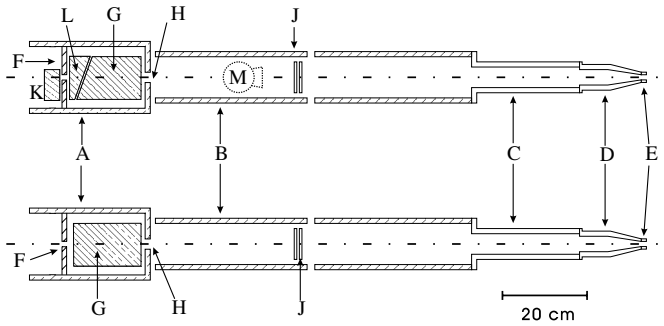

Figure 2. Comparison of the Harvard ocular nozzle (top, from Newhauser *et al* (2002)) and the simplified nozzle as modelled in MCNPX (bottom). Both renderings indicate the range shifter tube (A), the monitor chamber tube (B), the empty tube (C), the tapered snout (D), a 24 mm aperture (E), the first collimator with an inner diameter of 12.7 mm (F), a fixed degrader (G), the second collimator with an inner diameter of 25.4 mm (H), and the transmission ionization chambers (J). The upper diagram also illustrates the modulator wheel (K), the variable range shifter (L), and an x-ray tube (M) for patient set-up.

Table 1. Nozzle components, material and dimensions. There are four aluminium transmission monitor chamber plates within the nozzle, and each has a thickness of 0.25 mm and a radius of 25.4 mm. The inter-electrode gap between plates is 9.5 mm. Each chamber has a separation of 15 mm.

Component description	Material	Length (mm)	Outer radius (mm)	Inner radius (mm)
RM/RS tube	Brass	254	82.6	76.2
First collimator	Brass	10	76.2	6.4
Range shifter	Lexan	[a]	62.5	–
Second collimator	Brass	10	57.2	12.7
Monitor chamber tube	Brass	681	57.2	51.4
Monitor chamber plates	Aluminium	0.25	25.4	–
Empty tube	Brass	203	44.3	38.5
Tapered snout	Brass	161	44.3	[b]
Aperture	Brass	9.5	20	12

[a] The length of the range shifter can be adjusted within MCNPX, behaving like a combined range and variable degrader.
[b] The inner and outer radii of the snout change as the snout tapers into the final collimating aperture.

For simplicity, a complete range modulator wheel was not modelled in a single simulation. Instead, a series of separate simulations was carried out for each step of the range modulator wheel. The SOBP was subsequently obtained using the proton-fluence-weighted sum of the individual modulator step simulations. The range modulator material was modelled as a contiguous extension of the upstream end of the fixed degrader. The variable range shifter, which adjusts the maximum beam penetration range in the patient, was modelled by varying the length of the fixed degrader at its downstream face. This combined range modulator/shifter was assigned the composition and density of Lexan. Two air-filled, parallel-plate-type transmission ionization chambers (TIC1 and TIC2), commonly called monitor chambers, were included in the simulations. Downstream of these ion chambers, the protons again traverse air inside the snout, which holds the final collimating aperture. Two final collimating aperture designs were simulated: a 24 mm inside diameter circular aperture (referred to as the open aperture) and a hemi-circular aperture with a 26.3 mm inside diameter (referred to

as a half-beam block (HBB) aperture). After exiting the final collimating aperture, the proton beam traverses 57 mm of air before reaching the proximal surface of the phantom. A simple water phantom, $44 \times 44 \times 45$ mm^3, was used for the simulations.

Discrete tallies in the water phantom recorded the absorbed dose as a function of depth in 180 cylindrical cells, 5.4 mm in diameter and 0.25 mm thick, positioned on the beam's central axis. The cross-field absorbed dose profiles were simulated separately in a linear array of 0.8-mm-diameter spheres, 0.85 mm apart, centre-to-centre, with the sphere centres at a depth of 17.5 mm in the phantom.

2.2. Monte Carlo code, simulation parameters and geometry visualization

The MCNPX code from Los Alamos National Laboratory (MCNPX 2002a) is a general purpose Monte Carlo radiation transport code. The proton transport physics of MCNPX include energy straggling, multiple Coulomb scattering, elastic and inelastic scattering, and nonelastic nuclear reactions. Stopping power values were computed on-the-fly based on two models: the stopping power and range (SPAR) model (Armstrong and Chandler 1973) and the maximum kinetic energy transfer model (MCNPX 2002b), with shell corrections from Janni (1982) applied at intermediate energies. The default models were used for energy straggling (Vavilov 1957) and multiple Coulomb scattering based on the approach from Rossi and Greisen (1941). The low-energy proton transport cutoff was set at 1 MeV, below which the projectile trajectory is terminated and all remaining kinetic energy is deposited locally. The particles transported included protons, photons, pions, muons, ^{2}H, ^{3}H, ^{3}He and α particles. MCNPX allows the use of nuclear interactions that are read from evaluated cross-section library files (Chadwick *et al* 1999), and in cases where the evaluated cross-sections were not available, cross-sections were calculated on-the-fly using nuclear interaction models. For testing the sensitivity of the results to the choice of cross-section data, we compared dose distributions from simulations based exclusively on cross-section data libraries with those obtained from simulations based exclusively on cross-sections from nuclear model calculations. The nuclear interaction models used included elastic scattering of nucleons, the Bertini intranuclear cascade model, and a pre-equilibrium emission model after intranuclear cascades (see MCNPX (2002b) and references therein). For otherwise identical simulations, the different cross-section data yielded absorbed dose distributions that agreed with one another within 2% at any given depth. By adjusting the width of the distribution of initial proton energies, the differences vanished. Specifically, the nuclear model approach with an initial energy width of 3.53 MeV FWHM was statistically indistinguishable from the corresponding simulations based on cross-section library data and a 2.94 MeV FWHM. With the exception of this comparison, all of the simulations in this report relied on nuclear interaction data from nuclear models.

The cross-field profiles, owing to the relatively small volume of tally cells, required 110×10^6 particle histories to achieve relative statistical uncertainties (1-σ confidence interval) of about 1.25%, 1.75% and 5.5% at the central axis (CAX) and lateral 50% and 10% dose levels, respectively. The CAX per cent depth dose (PDD) profiles required 50×10^6 histories to achieve 0.5%, 0.7% and 2.4% relative uncertainties at the beam entrance and depths of the distal 90% and 10% dose levels, respectively. The simulations were carried out on a LINUX cluster with 22 nodes, each node containing a single, 1.8 GHz Pentium (Intel Corp, Santa Clara, CA) central processing unit (CPU). The simulation times for the cross-field profiles and depth-dose profiles, when expressed in calculation time on a single computer, were 24 days and 56 h, respectively. The complete set of simulations comprises six simulations

for cross-field profiles and 15 for PDD profiles. The total execution time for all simulations reported in this work was 4300 CPU-hours.

The MORITZ program (Van Riper 2003) (White Rock Science, Los Alamos, NM) facilitated the geometry creation and provided three-dimensional visualization of the ocular beamline. Within MORITZ, surfaces were created and then cells were created by specifying one or more bounding surfaces. The elemental composition and mass density values were assigned to each cell, along with a cell-specific variance-reduction parameter, or cell importance. Then, MORITZ automatically generated the geometry portion of the MCNPX input file.

2.3. Measurements

Measurements of absorbed dose distributions in the ocular proton therapy treatment field were carried out in order to characterize the therapy apparatus, to provide input data to the treatment planning system and to provide a basis to validate the dose predictions from the treatment planning system. The measurements were all carried out on the same ocular treatment nozzle, but during the course of this work the nozzle was moved from the Harvard Cyclotron Laboratory to its replacement facility, the Northeast Proton Therapy Center (NPTC, Boston, MA). This provided an opportunity to repeat some of the measurements, yielding additional information regarding the reproducibility of the dosimetric measurements.

At the NPTC, a CAX PDD profile of a pristine Bragg peak without range modulation was measured in a water phantom using a Markus parallel-plate ionization chamber (PTW, Model: 23342, SN: 2397, Freiburg, Germany). A separate thimble chamber (Exradin Inc, Model: T1, SN: 258, Middleton, WI) was stationary in the beam and served as a reference chamber to compensate for temporal fluctuations in the beam current.

The Bragg curve was measured using a range shifter setting that corresponded to a proton range setting of 25 mm in water, and a circular 24-mm-diameter final collimating aperture was installed. The distance between the downstream face of the aperture and the upstream face of the water tank was 57 mm, which corresponded to the typical distance separating the downstream aperture edge and the proximal face of the water phantom in calibration measurements (Newhauser *et al* 2001, 2002a). Similarly, a CAX PDD profile of a pristine Bragg peak with a range of 20 mm was also measured at Harvard, where this nozzle was in clinical service from 1975 to 2002, but instead using the silicon diode dosimeter described by Newhauser *et al* (2001, 2002a).

At NPTC, cross-field dose profiles were measured in five different unmodulated beams, with the nozzle's internal range shifter adjusted to provide a proton beam penetration depth of 20, 25, 30, 35 and 40 mm. These absorbed dose profiles were measured with a small-volume, air-filled ionization chamber (PTW Inc, Model: Pinpoint TN31006, SN: 0178, Freiburg, Germany). The dosimeter was placed 90 mm downstream of the HBB final collimating aperture. A Lucite slab of 17.5 mm water-equivalent thickness was introduced 10 mm upstream of the dosimeter to approximate the source-to-surface distance and the tumour depth for a typical ocular melanoma treatment. In addition, an open-field measurement was made at the NPTC with the range shifter set to deliver a beam with a range of 25 mm and an open aperture of 24 mm. The measurement conditions and experimental methods were otherwise identical to those of the HBB measurements.

Radiographic film measurements (Eastman Kodak Co, Model: X-Omat V Film, Rochester, NY) provided additional information about the cross-field relative dose distributions. These measurements were taken under conditions identical to those described above. The films were affixed to the downstream face of the Lucite slab. For the open-beam

(24-mm-diameter aperture) irradiation, approximately 0.5 Gy was delivered to the film. Measurements were carried out with the film located behind the HBB aperture in order to verify that the dosimetric properties, such as the lateral penumbral width, were similar in the horizontal and vertical directions. For these measurements, the irradiation conditions were identical except that the HBB aperture's orientation was rotated by 90°. The films were digitized with a 16 bit charged-coupled device (CCD) film scanner (VIDAR Systems Corporation, Model: VXR-16 DosimetryPRO, SN: 102318, Herndon, VA) using a resolution of 71 dots per inch (0.36 mm^2 pixel size). This CCD scanner measured the optical density (OD) across a profile perpendicular to each of the HBB orientations and in the x and y directions across the film exposed to the open field. The OD was converted to absorbed dose using a measured calibration curve.

2.4. Analysis and comparison of measured and simulated dose distributions

All measured dose profiles were normalized to unit value. The PDDs were normalized to the maximum value in the peak. The open-aperture cross-field dose profiles were all normalized by fitting a straight line with near-zero slope in the interval -10 mm $< x <$ 10 mm. The HBB profiles were similarly normalized, using the region within 4 mm $< x <$ 10 mm to avoid the dose gradients in the shoulder regions.

Measured and simulated data were compared using profile plots, ratios of the profiles, and absolute differences in the selected profile widths. The shapes of the CAX PDD and open-field cross-field profiles were compared qualitatively using plots and quantitatively using the figures of merit described below. In depth, the absolute widths of the Bragg peak at the 90%–90% and 80%–80% dose levels were compared. Ratios of the PDD data from Monte Carlo simulations and measurements were also examined. In the cross-field profiles, ratios of Monte Carlo to ionization chamber (IC) measurements and film measurements to IC measurements were compared. In addition, the absolute widths at the 90%–90%, 80%–80%, 50%–50%, 20%–20% and 10%–10% dose levels, as well as the lateral penumbral widths, e.g., the 90%–10% and 80%–20% widths, of the measured and simulated cross-field profiles were compared.

2.5. Virtual commissioning of the treatment planning system

We commissioned the EYEPLAN ocular treatment planning system originally developed by Goitein and Miller (1983). A more recent description of this system was reported by Adams *et al* (1999). In this work, we commissioned an enhanced derivative of this code from Sheen (2001). The commissioning comprised two main tasks: generating nozzle-specific parameters and dose profiles and entering them into the treatment planning system, and testing the accuracy of the planning system's dose predictions under various beam conditions that are representative of ocular melanoma treatments. Traditionally, this is accomplished exclusively with measured data. Because we relied exclusively on simulated data, we refer to this process as virtual commissioning. Figure 3 shows the virtual commissioning process schematically; two of the tasks, benchmarking against measurements and determining the source parameters, are described above. In the remainder of this section, we describe what data were required to commission the TPS, how these data were obtained from Monte Carlo simulations, and how the accuracy of the TPS dose predictions was tested against additional Monte Carlo simulations.

2.5.1. Input data required to configure the TPS. The TPS predicts absorbed dose with a very simple broad-beam algorithm that uses a combination of lookup tables and geometric scaling

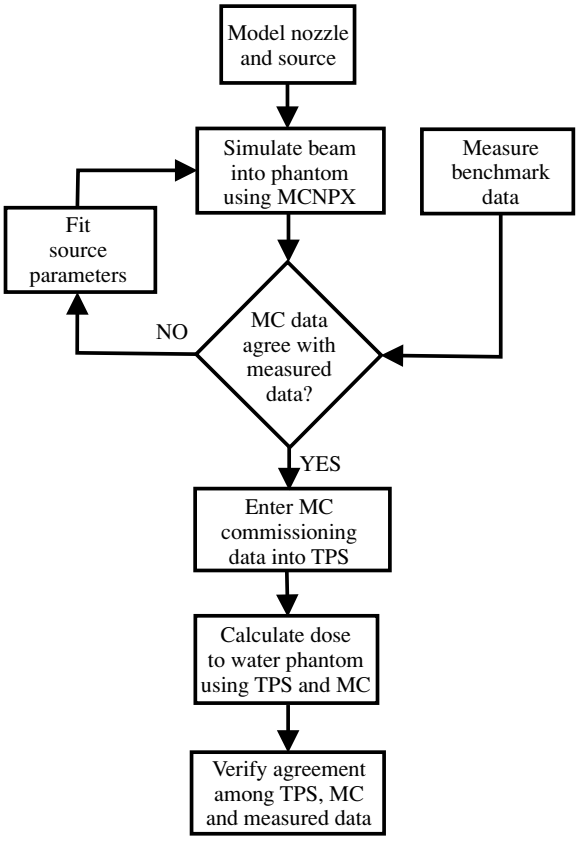

Figure 3. A flowchart illustrating the process of benchmarking the Monte Carlo results to measurements and the commissioning of EYEPLAN using Monte Carlo data. In practice, several iterations may be required in order to obtain sufficient agreement between simulated and measured results, particularly where measured parameter values are not available, such as the initial energy distribution of the raw proton beam.

techniques (Sheen 2001). The algorithm neglects the contribution to penumbral growth that is caused by multiple Coulomb scattering in the eye. Also, the planning system approximates the high-dose region of the spread-out Bragg peak as constant in value, i.e., the non-uniformities that can result from lateral scattering effects and ripples in the range modulation function are neglected. This simplistic approach offers the advantage of requiring relatively little input data to configure the algorithm. Specifically, these comprise two geometric parameters and three absorbed dose profiles. The required distances are that from the final collimating aperture and that from the virtual source to isocentre. The three absorbed dose profiles, which are used as lookup table data in the algorithm, include two in the depth direction and one in the cross-field direction, and they are obtained in an unmodulated proton field. These tables describe the proximal region from entrance to the peak, lateral penumbra, and distal falloff region for a single beam. The dose values in each of these tables are normalized such that the maximum dose has a unit value.

The absorbed dose profiles and the virtual source position were deduced from the results of the Monte Carlo simulations (see sections 2.1 and 2.2). The simulations were carried out for an unmodulated proton beam with 25 mm range in water and a circular field size of 24 mm

at the collimating aperture. The final collimating aperture position was set 74.5 mm upstream from the isocentre, based on a measurement of the Harvard nozzle dimensions (Newhauser *et al* 2001, 2002a). The virtual source position was estimated from cross-field profiles that were simulated in the open field at a 17.5 mm depth (in the isocentric plane) in the water phantom. The virtual source position was deduced from the similar triangles method, using the half-width at half-maximum (HWHM) field size at the tallying plane and the physical size of the collimating aperture, yielding a virtual source position of 1228 mm relative to the isocentre.

Prior to entering the lateral falloff curve into the TPS, it was shifted by 12.8 mm so that the 50% lateral falloff point occurred at a relative lateral position value of 0 cm. To cross-check the estimated virtual source location described above, we repeated the analysis for the HBB field and obtained a virtual source position of 1261 mm, which is in good agreement with the open-field result, considering the sensitivity of this calculation due to the small field sizes examined.

In configuring the TPS, the recommended approach is to enter the CAX dose data in a way that the SOBP width is defined by the distance from the proximal 100% dose point to the distal 90% dose point. However, we configured the TPS so that it produced SOBP widths specified by the distance from the proximal 90% depth to the distal 90% depth. The TPS developer (Sheen 2001, Sheen 2003–2004) recommended dividing the depth values (prior to entry into the lookup table) by a factor of 1.05 to take into account the slightly higher density (and correspondingly proton range) of eye tissue compared with water. However, we intentionally omitted this step in order to facilitate comparison of the dose distributions, which in this work were predicted exclusively in water.

2.5.2. Assessment of the TPS dose prediction accuracy. The accuracy of the TPS's relative dose predictions was verified by comparison with simulated dose distributions in a water phantom, including central-axis profiles and cross-field profiles at several water depths. Recall that the verification of the Monte Carlo model was accomplished through comparison with measurements (see section 2.3). The beam conditions, nozzle configuration and phantom geometry were identical for the EYEPLAN and MCNPX predictions.

Creating the simple geometric phantom in EYEPLAN was accomplished by using its existing anatomical modelling capability. Unlike most other conventional treatment planning systems, EYEPLAN does not use tomographic images of the patient anatomy for dose calculations. Instead, geometrical models of the eye, eyelid and tumour are adapted for each patient using dimensions from clinical measurements, e.g., fundus photographs, orthogonal x-rays and ultrasound images. Therefore, the flat-faced phantom was conveniently modelled by specifying that the skin plane, which anatomically corresponds to the surface of a patient's skin, lies just anterior of the cornea and producing a flat surface for the EYEPLAN phantom. The dose distributions were exported from the TPS in a two-dimensional square grid with a spatial resolution of 0.8 mm. The one-dimensional dose profiles were extracted from these dose matrices for comparison with the one-dimensional Monte Carlo profiles.

Dose profiles were compared under the following beam conditions: 25 mm range setting, 24-mm-diameter open aperture, 57 mm air gap and zero modulation. Cross-field profiles using the open aperture were taken at a depth of 17.5 mm in water along the isocentric plane. Also at this depth, separate cross-field profiles were simulated with the HBB aperture installed. Quantitative assessment of the agreement between the Monte Carlo and TPS predictions was as follows: for the CAX profiles, we compared the 90%–90% and 80%–80% peak widths, the 90%–10% and 80%–20% widths in the distal falloff region and the depth of the distal 90% point.

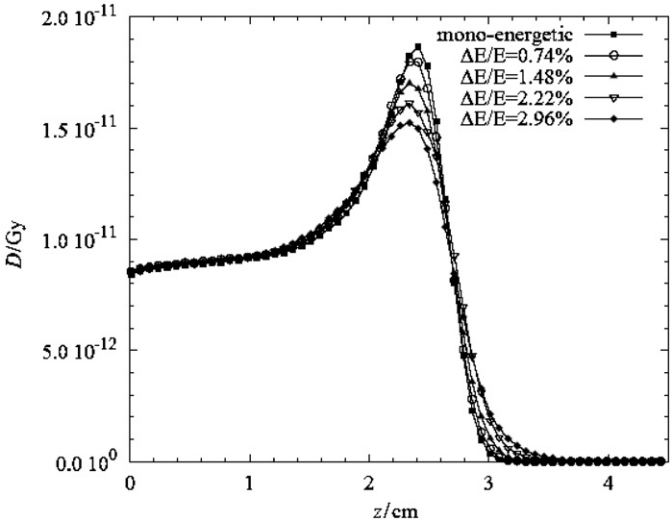

Figure 4. Simulated absorbed dose D per source proton as a function of water depth z along the beam's central axis for beams with an initial mean energy of 159 MeV and various initial energy distributions. The simulations reveal the differences in the shape of $D(z)$ for several initial proton energy distribution widths ranging from zero (mono-energetic beam) to a Gaussian distribution relative width of $\Delta E/E = 2.96\%$.

EYEPLAN assumes that changes in the penumbra are not significant in the small assortment of aperture sizes and ranges used in eye treatments. To investigate the validity of this assumption, the TPS cross-field dose calculations were compared to cross-field IC measurements and Monte Carlo simulation data for the HBB aperture for the ranges of 20, 25, 30, 35 and 40 mm. The cross-field widths, such as the 90%–90%, 80%–80%, 50%–50%, 20%–20% and 10%–10%, as well as lateral penumbral widths, e.g., 90%–10% and 80%–20%, were compared at a depth of 17.5 mm in water. Film measurements of the open field and HBB apertures were also compared. The widths at these dose levels were linearly interpolated from data points spaced about 0.8 mm apart for both the TPS and Monte Carlo profiles. For the HBB profiles, the lateral penumbra widths were taken from the off-axis field edge, whereas for the circular open fields these widths were averaged.

3. Results

3.1. Determination of $\Delta E/E$ value

Figure 4 plots the simulated central axis depth–dose curves, revealing the influence of the width of the raw beam's energy spread on the shape of the pristine Bragg curve. A comparison of these simulations with measurements from Harvard and the NPTC revealed that an initial relative beam energy width, $\Delta E/E$, equal to 2.22% ($\Delta E = 3.53$ MeV FWHM) provided good agreement in the shape of the simulated and measured Bragg curves, as is apparent in figure 5. Recall from section 2.2 that a good agreement was obtained between simulations using the evaluated nuclear cross-section library and those using the nuclear models, but the ΔE was decreased to 2.94 MeV FWHM ($\Delta E/E = 1.84\%$) for the former simulations. No measurements of the $\Delta E/E$ value for the Harvard ocular beamline are known to exist. However, both of our $\Delta E/E$ values are only slightly larger than the measured value of

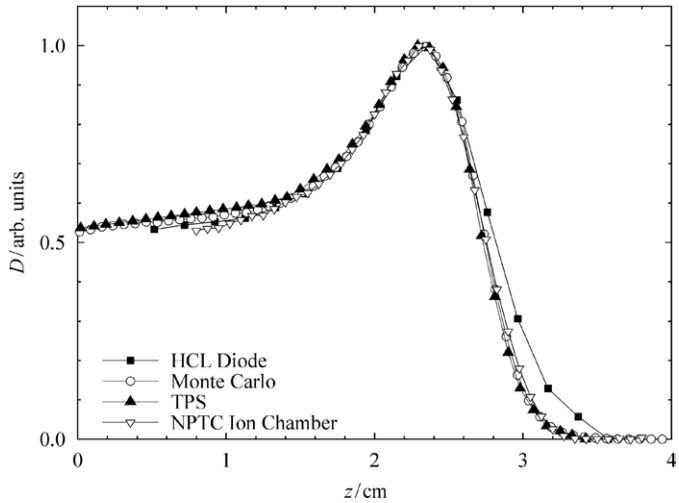

Figure 5. Comparison of central axis absorbed dose D as a function of water depth z where data are from a diode measurement at the Harvard Cyclotron Laboratory (HCL), an MCNPX-based simulation model, the EYEPLAN treatment planning system, and an ionization chamber measurement from the Northeast Proton Therapy Centre (NPTC). The MCNPX simulation is with a Gaussian initial proton beam energy distribution (mean energy of 159 MeV, $\Delta E/E = 2.22\%$). The HCL, EYEPLAN and NPTC curves were offset in z by 4.6 mm, 0.2 mm and −0.13 mm, respectively, to force the distal 90% point to a 25 mm water depth.

Table 2. Pristine Bragg curve characteristics as a function of the standard deviation of the Gaussian initial energy distribution σ_E or $\Delta E/E$. This table lists the peak dose per proton (D_P/p), the peak-dose-to-entrance-dose ratio (D_P/D_E), the peak width ($z_{D90} - z_{P90}$) and the distance from the distal 80% to the distal 20% points ($z_{D20} - z_{D80}$).

σ_E (MeV)	$\Delta E/E$ (%)	D_P/p (Gy × 10^{-11})	D_P/D_E	$z_{D90} - z_{P90}$ (mm)	$z_{D20} - z_{D80}$ (mm)
0.00	0.00	1.87	2.22	2.8	2.4
0.25	0.37	1.85	2.17	2.9	2.5
0.50	0.74	1.81	2.12	3.0	2.7
0.75	1.11	1.75	2.06	3.3	2.9
1.00	1.48	1.70	2.00	3.5	3.0
1.25	1.85	1.66	1.95	3.6	3.2
1.50	2.22	1.62	1.90	3.8	3.4
1.75	2.59	1.57	1.85	4.0	3.5
2.00	2.96	1.53	1.78	4.3	3.8
2.25	3.33	1.50	1.76	4.5	3.9

1.18 MeV FWHM (0.73%) reported by Gottschalk *et al* (1999) in Harvard's large-field beamline.

Table 2 summarizes several parameters that quantify the influence of $\Delta E/E$ on the following properties of the simulated Bragg curve: peak dose per proton, peak-to-entrance absorbed dose ratio, width of the Bragg peak (proximal 90% to distal 90%) and distal falloff width (80% to 20%). As the initial relative proton energy width, $\Delta E/E$, increased from 0% to 3.33%, the peak dose per proton decreased by 20%. As $\Delta E/E$ was increased, the distance between the proximal 90% and the distal 90% points increased by 1.7 mm, from 2.8 mm to

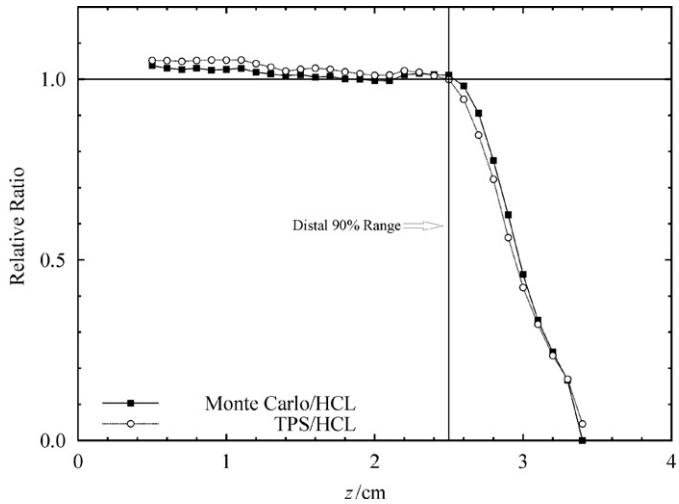

Figure 6. Ratios of the Monte Carlo and EYEPLAN treatment planning system (TPS) depth dose predictions to the corresponding measurements at the Harvard Cyclotron Laboratory (HCL) as a function of phantom depth z. These are ratios of curves shown in figure 5. The vertical line at 2.5 cm depth corresponds to the distal 90% point.

4.5 mm. The distance from the distal 80% point to the distal 20% point increased by 1.5 mm, from 2.4 mm to 3.9 mm. The entrance dose is nearly independent of the initial energy spread.

3.2. Verification of the Monte Carlo model with measurements

Figure 5 plots the simulated and measured central axis Bragg curves. Figure 6 plots the ratio of the simulated to measured Bragg curves, where the measurement is from Harvard. Figure 7 plots the corresponding ratio where the measurement is from the NPTC. Both figures 6 and 7 reveal that the Monte Carlo simulations are in good agreement with the measured profiles in the water phantom, i.e., the maximum difference at a given depth is less than 4% and 6% at depths up to 25 mm, respectively. In the distal falloff region, i.e., beyond 25 mm depth, the agreement between simulated and measured curves is characterized in terms of the difference of the distal-80%-to-distal-20% widths. Excellent agreement was found, with 80%–20% widths of 4.9 mm in the Harvard diode measurement, 3.8 mm in the NPTC ionization chamber measurement and 3.4 mm in the Monte Carlo simulation. The distal falloff width is larger in the Harvard measurement compared with the NPTC measurement due to radiation damage incurred in the fixed degrader at Harvard. The fixed degrader was replaced after the measurements at Harvard were taken and before the measurement at NPTC. The agreement in the width of the Bragg peak is also good, as shown in figure 5, with the simulated 90%–90% and 80%–80% widths within 0.2 mm of the corresponding measurements. This agreement is mainly determined by the $\Delta E/E$ value selected for simulations (discussed in section 3.1).

Figure 8 plots the Monte-Carlo-predicted and measured open-beam cross-field absorbed dose profiles, revealing generally good agreement, with the following noteworthy exceptions. The ionization chamber measurement differs from the other three profiles in the shoulder region and in the toe region. The IC's spatial resolution, which is inferior to that of the other dosimeters and of the simulation tallies, resulted in a smearing effect that was only apparent at the shoulder.

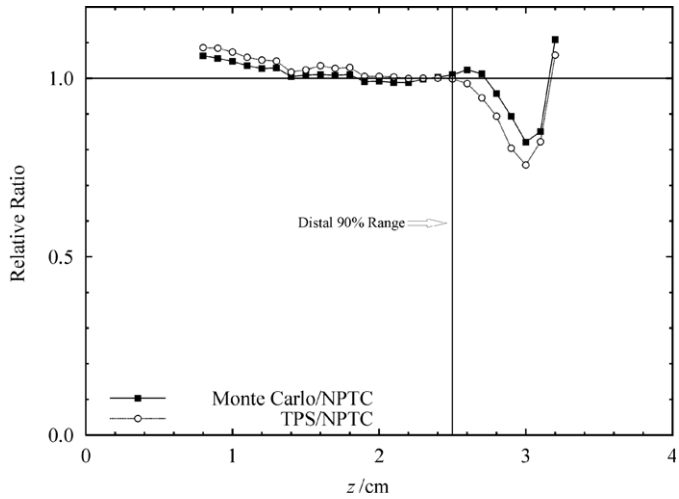

Figure 7. Ratios of the Monte Carlo and EYEPLAN treatment planning system (TPS) depth dose predictions to the corresponding measurements from the Northeast Proton Therapy Center (NPTC) as a function of phantom depth z. These are ratios of the curves shown in figure 5. The vertical line at 2.5 cm depth corresponds to the distal 90% point.

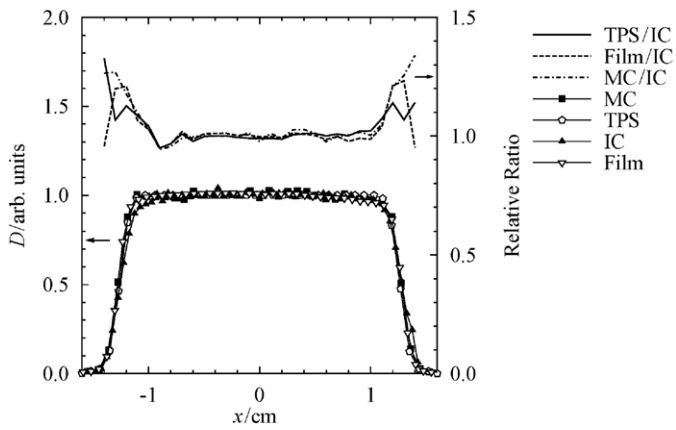

Figure 8. (Left abscissa) Monte Carlo (MC) simulations and measurements of proton absorbed dose as a function of cross-field location x. The open-field dose profiles are at a phantom depth of 17.5 mm where the beam penetration range in the phantom is 25 mm. A good agreement between all modalities was observed in the penumbral regions. (Right abscissa) Ratio of cross-field dose profile where the profiles are from the treatment planning system (TPS) predictions, film measurements, Monte Carlo (MC) simulations and ionization chamber (IC) measurements plotted in the upper graph.

Figure 8 also plots the ratio of the Monte-Carlo-predicted cross-field dose profile to that from IC measurements, more clearly revealing the agreement in the in-field and penumbral regions. In order to provide some assessment of the reliability of the IC measurements, we also compared the agreement between IC and film measurements. In figure 8, the ratio of film and IC profiles reveal approximately 2% differences between the profiles at various positions in the central region of the field, approximately 20% differences in the shoulder region, and more substantial differences in the outer penumbral regions. Figure 8 reveals the similarity

Table 3. Cross-field widths of an unmodulated proton beam with a range of 25 mm though a 24-mm-diameter final collimating aperture as predicted by a treatment planning system (TPS), measured with an ion chamber (IC) or film, and simulated with a Monte Carlo (MC) radiation transport technique.

Range		Open field width characteristics (mm)					Penumbra (mm)	
(mm)	Source	90%–90%	80%–80%	50%–50%	20%–20%	10%–10%	80%–20%	90%–10%
25	TPS	23.3	24.1	25.5	26.8	27.7	1.3	2.2
	IC	22.4	23.3	25.1	26.9	27.5	1.8	2.6
	MC	23.4	24.2	25.6	26.9	27.7	1.4	2.2
	Film	23.2	23.9	25.2	26.4	27.2	1.3	2.0

Table 4. Cross-field profile widths of an unmodulated proton beam with ranges of 20, 25, 30, 35 and 40 mm through a semicircular half-beam block (HBB) with a radius of 13.1 mm, as predicted by a treatment planning system (TPS), measured with an ion chamber (IC) or film, and simulated with a Monte Carlo (MC) radiation transport technique.

							Penumbra (mm)			
Range		Half-beam block field width characteristics (mm)					Field edge		Central axis	
(mm)	Source	90%–90%	80%–80%	50%–50%	20%–20%	10%–10%	80%–20%	90%–10%	80%–20%	90%–10%
20	TPS	11.8	12.6	13.9	15.3	16.2	1.7	2.3	1.0	2.0
	IC	11.8	12.6	14.3	15.9	16.8	1.7	2.6	1.6	2.3
	MC	11.5	12.4	13.9	15.4	16.2	1.6	2.4	1.5	2.3
25	TPS	11.8	12.6	13.9	15.3	16.2	1.7	2.3	1.0	2.0
	IC	11.8	12.7	14.2	15.7	16.4	1.6	2.5	1.4	2.1
	MC	12.0	12.7	14.1	15.5	16.2	1.5	2.3	1.4	2.1
	Film (X)	12.1	12.8	14.2	15.5	16.3	1.4	2.2	1.3	2.0
	Film (Y)	11.7	12.5	14.0	15.5	16.4	1.6	2.6	1.4	2.2
30	TPS	11.8	12.6	13.9	15.3	16.2	1.7	2.3	1.1	2.0
	IC	11.9	12.7	14.1	15.5	16.1	1.5	2.2	1.3	2.0
	MC	11.9	12.6	14.1	15.4	16.1	1.4	2.2	1.3	2.0
35	TPS	11.8	12.6	13.9	15.3	16.2	1.7	2.3	1.0	2.0
	IC	12.0	12.8	14.1	15.4	16.1	1.4	2.1	1.2	1.9
	MC	11.8	12.6	14.0	15.3	15.9	1.4	2.2	1.3	1.9
40	TPS	11.8	12.6	13.9	15.3	16.2	1.7	2.3	1.1	2.0
	IC	12.1	12.8	14.2	15.4	16.1	1.3	2.1	1.3	1.9
	MC	12.0	12.7	14.0	15.2	15.8	1.3	2.2	1.2	1.6

in shape between the Monte-Carlo-to-IC and the film-to-IC curves. Table 3 summarizes the lateral field widths for the curves shown in figure 8. The widths include the distances between the 90%–90%, 80%–80%, 50%–50%, 20%–20% and 10%–10% dose levels and the 90%–10% and 80%–20% dose levels in the penumbra. A maximum difference of 1.0 mm between the Monte Carlo and IC measurements was observed at the 90%–90% cross-field width. The corresponding film measurement agreed with the Monte Carlo simulation to within 0.2 mm.

Table 4 lists the lateral penumbral and field widths from the HBB cross-field profiles of the Monte Carlo simulations and measurements. The off-axis 80%–20% and 90%–10%

penumbral widths from the measurements and simulations were all within 0.4 mm and 0.5 mm of one another, respectively. The corresponding values for central axis penumbral widths were within 0.4 mm and 0.6 mm, respectively. The maximum difference between the Monte Carlo and IC measurements of the lateral field width was 0.6 mm, which occurred once for the 20-mm-range beam at the 10%–10% dose level.

3.3. Verification of the treatment planning system with simulations and measurements

The TPS dose predictions were in good agreement with the Monte Carlo simulations. Figure 5 plots the normalized Bragg curves from the Monte Carlo simulation, the TPS's analytical model, and the IC and diode measurements. The ratio of the relative Bragg curves from the TPS and Monte Carlo simulations agrees within 3% at any depth from the entrance region to a depth of 26 mm. From 14 mm to 25 mm in depth, the corresponding agreement is within 1.2%. At greater depths, well past the peak of the Bragg curve where the dose is small and decreasing rapidly, the dose ratio increasingly deviates from unity.

The agreement of the TPS predicted dose profiles with measurements is also good. The ratio of the TPS's predicted Bragg curve to that of the corresponding measurement from NPTC reveals better than 3.5% agreement from a water depth of 14 mm to 25 mm. At deeper water depths, the ratio deviates from unity by up to 25%. The 80%–20% widths obtained were 3.4 mm with the TPS, 3.4 mm with the simulation and 3.8 mm with the NPTC IC measurement. The width predicted by the TPS was 1.5 mm and 0.4 mm smaller than the widths measured at Harvard and NPTC, respectively, which can be considered good agreement. The TPS predicts significantly a smaller distal falloff width when compared with the measured value from Harvard, which was due to range mixing caused by radiation damage to the Harvard fixed degrader (see section 3.2.1). The cross-field profiles from the TPS predictions and the simulations and measurements are in good agreement, as shown in figure 8. Figure 8 plots the ratio of TPS cross-field dose profiles to IC measurements, showing good agreement in the central region but deviations of up to approximately 15% at the 50% falloff point. Below the 50% dose level in the penumbral regions, the level of agreement between the TPS and IC deteriorates substantially, which has been discussed in section 3.2.2. Table 3 summarizes the TPS predictions, along with measured and simulated values, of the lateral characteristics of the open field at the isocentric plane in a phantom at a depth of 17.5 mm. Widths are specified at various relative dose points, i.e., from the 90%–90% width to the 10%–10% width. The TPS width predictions are within 0.4 mm of the measurement and within 0.1 mm of the open aperture simulation value. Table 3 also lists the 80%–20% and 90%–10% penumbral widths from measurements and simulations of the open aperture. All widths predicted by the TPS agree to within 0.2 mm of the film measurement and 0.1 mm of the simulations. Similarly, table 4 lists the values of the TPS predictions, Monte Carlo simulations, and IC and film measurements for the HBB-field radius. These penumbral widths are listed for beam penetration depths in the phantom in the interval from 20 mm to 40 mm.

The TPS does model geometric magnification of the penumbral width but does not attempt to model penumbral growth due to multiple Coulomb scattering within the phantom. In addition, the TPS does not model penumbral size as a function of the off-axis distance to the field edge. Despite these approximations, the accuracy of the TPS predictions of the penumbral width was adequate, i.e., within 0.4 mm of the measurements and 0.2 mm of the simulations in all of the cases considered above. Similarly, the TPS predictions of (50%–50%) field size were within 0.4 mm of the measurements and 0.4 mm of the simulations in all the cases considered. The differences between the TPS prediction values and IC measurements of the HBB field size as a function of beam penetration range are in all cases, within 0.6 mm.

The TPS increasingly underestimates the 80%–20% penumbral width with increasing beam penetration.

4. Discussion

In this work, we demonstrated that Monte Carlo predictions faithfully reproduce measured dose distributions in a phantom. At any given depth, the predicted and measured relative central axis-depth dose values differed at most by 6% (at the shallowest depths) and typically differed by only 2%. The distal 80%-to-20% falloff widths agreed to within 0.4 mm. The simulated open-field lateral dose profiles agreed with film measurements to better than 0.5 mm. Typically, the treatment margins are 2.5 mm distally and 1.5 mm laterally (cf Egger *et al* (2003)), and the positioning uncertainties in the measurements are approximately 0.2 mm. From this we conclude that the Monte Carlo method is sufficiently accurate for commissioning an ocular treatment planning system.

To our knowledge, this work represents the first demonstration that the Monte Carlo technique can generate a complete set of dosimetric required to commission and validate a proton therapy treatment planning system. Beyond this proof of principle exercise, we have learned several broadly applicable lessons. First, the flexibility of general purpose Monte Carlo codes, combined with the complexity of proton therapy systems, provides almost unlimited potential for introducing significant modelling errors. Hence, we emphasize the necessity for careful validation measurements in any clinical implementation of the Monte Carlo method. Second, the success of this proof-of-principle test suggests that simulations can, and likely will, play an increasingly important role when compared with measurements. Third, we find that simulation execution time remains a significant obstacle in the path to the ubiquitous application of Monte Carlo in proton radiotherapy.

While the total of 4300 CPU hours required for this study was substantial, if we were to carry out the study again today, the total elapsed time would be approximately 22 h, if the simulations were run in parallel on a 100-node cluster of 3.2 GHz Pentium computers. This estimate does not include recent efficiency improvements in the MCNPX code that have been implemented since our simulations were completed. We may conclude that the total computation time of less than one day is acceptable for clinical commissioning purposes and, in fact, is comparable to the time required to carry out the corresponding measurements. In a separate work (Koch and Newhauser 2005), we report similar total time requirements in a proton beam commissioning study. Therefore, we also conclude that the Monte Carlo simulations provide a feasible approach to generate clinical commissioning data, provided that the simulation model has been adequately benchmarked against measurements. The simulation methods reported in this study may be applied to any proton therapy nozzle.

Although the findings of this study are applicable to other proton beamlines, several limitations warrant mention. Most importantly, this work comprehensively studied unmodulated beams, whereas for clinical use, EYEPLAN would best be commissioned using SOBP dose profiles. In addition, we studied only an initial beam energy of 159 MeV, as was used at Harvard and is still used at NPTC. However, many ocular nozzles accept proton beams with energies below 100 MeV. We investigated these topics in a subsequent study that supports the same general findings reported here (Koch and Newhauser 2005). Specifically, we found that the Monte Carlo method is suitable for predicting the proton therapy dose for routine treatment planning. Computation times remain long compared to those of analytical methods, and dramatic decreases in simulation times are necessary. Steady increases in computing power are occurring, however, and we anticipate that enhancements to the Monte Carlo codes will

further increase efficiency. In this work, we have not applied variance reduction techniques, which we anticipate will also substantially reduce the calculation times.

Measurement-based commissioning processes are also time-consuming and expensive, and they cannot be carried out until the proton beam delivery equipment is operational. Simulations, on the other hand, may be completely automated and, therefore, will eventually become faster and less expensive than measurements. Furthermore, the simulation methods given here make possible prospective equipment design options, i.e., without the need to fabricate prototype equipment or to take measurements (Koch and Newhauser 2005). This is significant because many clinically important aspects of the nozzle design are difficult or impossible to study prospectively using analytical models, e.g., the local shielding to protect patients from stray radiation, and the effects of beam mis-steering on field flatness, to name a few. In light of these advantages, we anticipate that Monte Carlo simulations will play the predominant role in future commissioning and design work. A limited set of measurements will always be needed to verify the accuracy of new or revised simulation models.

One of the main impediments to the widespread adoption of Monte Carlo simulation methods for clinical and design applications is the time and expense associated with developing and benchmarking a simulation model. The availability of sample simulation models and benchmarking data would largely solve these problems. Benchmarking data should include dose distributions in a water phantom, dose distributions in heterogeneous phantoms, proton fluence in air parallel and perpendicular to the beam axis, and neutron dose equivalent distributions near the isocentre. Additional experimental data will be required for the latest generation of proton therapy beam delivery systems now entering service.

Finally, the present findings on the analytical algorithm's dose prediction accuracy are applicable only to this particular TPS's dose model. Specifically, the limitations on accuracy reported here are predominated by the ultra-simple *implementation* of EYEPLAN's broad beam algorithm, not by the broad beam approach itself. For example, the TPS's prediction of lateral dose falloff could be improved by taking into account the penumbral growth due to multiple Coulomb scattering in the patient using, for example, the methods for either broad-beam or pencil-beam algorithms given by Hong *et al* (1996). Many additional improvements to analytical proton dose models have been reported including those by Russell *et al* (2000), Schaffner *et al* (1999) and Szymanowski *et al* (2002). In many clinical situations, but importantly not in all, the pencil beam's inherent accuracy in predicting proton absorbed dose in the patient approaches that of the Monte Carlo method (cf Tourovsky *et al* (2005)). Hence, their main advantage is the high execution speed needed for routine treatment planning. It appears likely that proton therapy clinics will continue to rely mainly on analytical dose models until Monte Carlo methods become sufficiently fast, which we estimate will occur in five to ten years from now. The preponderance of recent literature, including this work, suggests that the Monte Carlo method will become ubiquitous in proton therapy clinics, eventually replacing contemporary analytical dose algorithms in the majority of applications.

5. Conclusions

Monte Carlo simulations can and should be used in commissioning ocular proton therapy treatment planning systems. The accuracy of Monte Carlo simulations is superior to that of EYEPLAN, the most widely used ocular proton treatment planning system. Computation times are reasonably short when carried out on a parallel computing cluster and are comparable with measurement times. Our results also suggest that the MCNPX Monte Carlo code would be suitable for routine treatment planning dose calculations once the simulation model is

encapsulated and integrated into a treatment planning system. We expect that these techniques will be used for nozzle design work, dose-per-monitor-unit predictions and, eventually, routine treatment planning.

Acknowledgments

We would like to express our gratitude to Dr Radhe Mohan and Mr Stan Bujnowski for providing support with the parallel computing infrastructure. This work was supported by The University of Texas M D Anderson Cancer Center through a faculty development grant, by Varian Medical Systems, Inc, through a research grant, and by the Sam Taub and Beatrice Burton Endowment through a research fellowship.

References

Adams J, Paiva K, Munzenrider J, Miller J and Gragoudos E 1999 Proton beam therapy for age-related macular degeneration: development of a standard plan *Med. Dosim.* **24** 233–8

Agosteo S, Birattari C, Caravaggio M, Silari M and Tosi G 1998 Secondary neutron and photon dose in proton therapy *Radiother. Oncol.* **48** 293–305

Armstrong T W and Chandler K C 1973 *SPAR, A FORTRAN Program for Computing Stopping Powers and Ranges for Muons, Charged Pions, Protons and Heavy Ions* ORNL-4869, Oak Ridge, TN: Oak Ridge National Laboratory

Bues M, Newhauser W D, Titt U and Smith A R 2005 Proton beam shaping with a multi-leaf collimator: a Monte Carlo study *Radiat. Prot. Dosim.* at press

Chadwick M B *et al* 1999 Cross-section evaluations to 150 MeV for accelerator-driven systems and implementation in MCNPX *Nucl. Sci. Eng.* **131** 293–328

Constable I J and Koehler A M 1974 Experimental ocular irradiation with accelerated protons *Invest. Ophthalmol.* **13** 280–7

Egger E, Zografos L, Schalenbourg A, Beati D, Borhringer T, Chamot L and Goitein G 2003 Eye retention after proton beam radiotherapy for uveal melanoma *Int. J. Radiat. Oncol. Biol. Phys.* **55** 867–80

Fippel M and Soukup M 2004 A Monte Carlo dose calculation algorithm for proton therapy *Med. Phys.* **31** 2263–73

Fontenot J, Newhauser W D and Titt U 2005 Design tools for proton therapy nozzles based on the double-scattering foil technique *Radiat. Prot. Dosim.* at press

Goitein M and Miller T 1983 Planning proton therapy of the eye *Med. Phys.* **10** 275–83

Gottschalk B, Platais R and Paganetti H 1999 Nuclear interactions of 160 MeV protons stopping in copper: a test of Monte Carlo nuclear models *Med. Phys.* **26** 2597–601

Gragoudas E and Lane M 2005 Uveal melanoma: proton beam irradiation *Opthal. Clin. N. Am.* **18** 111–8

Hérault J, Iborra N, Serrano B and Chauvel P 2005 Monte Carlo simulation of a proton therapy platform devoted to ocular melanoma *Med. Phys.* **32** 910–9

Hong L, Goitein M, Bucciolini M, Comiskey R, Gottschalk B, Rosenthal S, Serago C and Urie M 1996 A pencil beam algorithm for proton dose calculations *Phys. Med. Biol.* **41** 1305–30

Hughes G, Prael R and Little R 1997 MCNPX—the LAHET/MCNP code merger *Technical Report* LA-UR-97-4891, Los Alamos National Laboratory, USA

Janni J F 1982 Proton range-energy tables, 1 keV–10 GeV—energy loss, range, path length, time-of-flight, straggling, multiple scattering and nuclear interaction probability *At. Data Nucl. Data Tables* **27** 147–339 and 341–527

Jiang H and Paganetti H 2004 Adaptation of GEANT4 to Monte Carlo dose calculations based on CT data *Med. Phys.* **31** 2811–8

Koch N and Newhauser W 2005 Virtual commissioning of a treatment planning system for proton therapy of ocular cancers *Radiat. Prot. Dosim.* at press

MCNPX Team at Los Alamos National Laboratory 2002a MCNPX version 2.3.0 *Technical Report* LA-UR-02-2607, Los Alamos National Laboratory, USA

MCNPX Team at Los Alamos National Laboratory 2002b MCNPX version 2.4.k *Technical Report* LA-CP-02-408, Los Alamos National Laboratory, USA

Medin J and Andreo P 1997 Monte Carlo calculated stopping-power ratios, water/air, for clinical proton dosimetry (50–250 MeV) *Phys. Med. Biol.* **42** 89–105

Mourtada F, Koch N and Newhauser W D 2005 Ruthenium-106 eye plaque and proton radiotherapy for ocular melanoma: a comparative dosimetric study *Radiat. Prot. Dosim.* at press

Munzenrider J *et al* 1989 Conservative treatment of uveal melanoma: local recurrence after proton beam therapy *Int. J. Radiat. Oncol. Biol. Phys.* **17** 493–8

Newhauser W D, Burns J and Smith A 2001 Proton beam dosimetry part V: ocular dosimetry at the Harvard Cyclotron Laboratory based on the IRCU Report 59 *Northeast Proton Therapy Center Report Number* NPTC-HD-109

Newhauser W D, Myers K, Rosenthal S and Smith A 2002a Proton beam dosimetry for radiosurgery: implementation of the ICRU Report 59 at the Harvard Cyclotron Laboratory *Phys. Med. Biol.* **47** 1369–89

Newhauser W D, Titt U, Dexheimer D, Yan X and Nill S 2002b Neutron shielding verification measurements and simulations for a 235-MeV proton therapy center *Nucl. Instrum. Methods* A **476** 80–4

Paganetti H 1998a Calculation of the spatial variation of relative biological effectiveness in a therapeutic proton field for eye treatment *Phys. Med. Biol.* **43** 2147–57

Paganetti H 1998b Monte Carlo method to study the proton fluence for treatment planning *Med. Phys.* **25** 2370–5

Paganetti H, Jiang H, Adams J A, Chen G T and Rietzel E 2004a Monte Carlo simulations with time-dependent geometries to investigate effects of organ motion with high temporal resolution *Int. J. Radiat. Oncol. Biol. Phys.* **60** 942–50

Paganetti H, Jiang H, Lee S Y and Kooy H M 2004b Monte Carlo simulations for nozzle design, commissioning and quality assurance for a proton radiation therapy facility *Med. Phys.* **31** 2107–18

Palmans H, Symons J E, Denis J M, de Kock E A, Jones D T and Vynckier S 2002a Fluence correction factors in plastic phantoms for clinical proton beams *Phys. Med. Biol.* **47** 3055–71

Palmans H, Verhaegen F, Denis J M and Vynckier S 2002b Dosimetry using plane-parallel ionization chambers in a 75 MeV clinical proton beam *Phys. Med. Biol.* **47** 2895–905

Polf J C and Newhauser W D 2005 Effect of range modulation on the neutron dose equivalent around a passive scattering proton therapy treatment nozzle *Phys. Med. Biol.* **50** 3859–73

Polf J C, Newhauser W D and Titt U 2005a Patient neutron dose equivalent exposures outside the proton therapy treatment field *Radiat. Prot. Dosim.* at press

Polf J C, Newhauser W D and Titt U 2005b Calculations of neutron dose equivalent values for the proton spot-scanning nozzle at the M. D. Anderson Proton Therapy Center *Radiat. Prot. Dosim.* at press

Prael R and Lichtenstein H 1989 User's Guide to LCS: The LAHET Code System *Technical Report* LA-UR-89-3014 Los Alamos, NM, Los Alamos National Laboratory

Romero J L *et al* 1995 Patient positioning for protontherapy using a proton range telescope *Nucl. Instrum. Methods* A **356** 558–65

Rossi B and Greisen K 1941 Cosmic-ray theory *Rev. Mod. Phys.* **13** 240–70

Russell K, Isacsson U, Saxner M, Ahnesjö A, Montelius A, Grusell E, Vallhagen Dahlgren C, Lorin S and Glimelius B 2002 Implementation of pencil kernel and depth penetration algorithms for treatment planning of proton beams *Phys. Med. Biol.* **45** 9–27

Sakae T, Nohtomi A, Maruhashi A, Sato M, Terunuma T, Kohno R, Akine Y, Hayakawa Y and Koike Y 2000 Multi-layer energy filter for realizing conformal irradiation in charged particle therapy *Med. Phys.* **27** 368–73

Schaffner B, Pedroni E and Lomax A 1999 Dose calculation models for proton treatment planning using a dynamic beam delivery system: an attempt to include density heterogeneity effects in the analytical dose calculation *Phys. Med. Biol.* **44** 27–41

Schneider U, Agosteo S, Pedroni E and Besserer J 2002 Secondary neutron dose during proton therapy using spot scanning *Int. J. Radiat. Oncol. Biol. Phys.* **53** 244–51

Schulte R W, Bashkirov V, Loss Klock M C, Li T, Wroe A J, Evseev I, Williams D C and Satogata T 2005 Density resolution of proton computed tomography *Med. Phys.* **32** 1035–46

Sheen M 2001 EYEPLAN User Manual v. 3.01 Douglas Cyclotron Laboratory, Clatterbridge, England

Sheen M 2003–2004 Personal electronic communications

Siebers J 2000 Application of Monte Carlo to proton therapy radiation therapy *Proc. from Advanced Monte Carlo for Radiation Physics, Particle Transport Simulations, and Applications (Lisbon, 23–6 Oct.)* ed A Kling, F Barão, M Nakagawa, L Távora and P Vaz (New York: Springer) pp 1051–6

Sisterson J 2003 Particles Newsletter *Proton Therapy Co-Operative Group* **31** 10 (http://ptcog.mgh.harvard.edu/Particles%2031.pdf)

Stallard H B 1968 Malignant melanoblastoma of the choroid *Bibl. Ophthalmol.* **75** 16–38

Szymanowski H and Oelfke U 2002 Two-dimensional pencil beam scaling: an improved proton dose algorithm for heterogeneous media *Phys. Med. Biol.* **47** 3313–30

Titt U and Newhauser W D 2005 Neutron shielding in a proton therapy facility based on Monte Carlo simulations: the design method of choice *Radiat. Prot. Dosim.* at press

Tourovsky A, Lomax A J, Schneider U and Pedroni E 2005 Monte Carlo dose calculations for spot scanned proton therapy *Phys. Med. Biol.* **50** 971–81

Urie M, Sisterson J, Koehler A, Goitein M and Zoesman J 1986 Proton beam penumbra: effects of separation between patient and beam modifying devices *Med. Phys.* **13** 734–41

Van Riper K 2003 *Moritz User's Manual Version W98_VR_0.85, 2000–2003* (White Rock, NM: White Rock Science)

Vavilov P V 1957 Ionization losses of high-energy heavy particles *Sov. Phys.—JETP* **5** 749

Verhaegen F and Palmans H 2001 A systematic Monte Carlo study of secondary electron fluence perturbation in clinical proton beams (70–250 MeV) for cylindrical and spherical ion chambers *Med. Phys.* **28** 2088–95

Wilson R 1946 Radiological use of fast protons *Radiology* **47** 487–91

Wroe A J, Cornelius I M and Rosenfeld A B 2005 The role of nonelastic reactions in absorbed dose distributions from therapeutic proton beams in different medium *Med. Phys.* **32** 37–41

Yan X, Titt U, Koehler A and Newhauser W 2002 Measurement of neutron dose equivalent to proton therapy patients outside of the proton radiation field *Nucl. Instrum. Methods* A **476** 429–34